

Electroproduction of Kaons up to $Q^2=3 \text{ (GeV/c)}^2$

P. Markowitz. M. Iodice,

S. Frullani, C.C. Chang,

O.K. Baker

Hall A Collaboration Proposal

Florida International University, Miami, Florida

INFN - Sanita', Roma, Italy

University of Maryland, College Park, Maryland

Hampton University, Hampton, Virginia *CEBAF, Newport News, Virginia*

The George Washington University, Washington D.C.

MIT, Cambridge Massachusetts

North Carolina A&T State University, Greensboro, NC

The Rutgers University, Piscataway, New Jersey

The University of Virginia, Charlottesville, Virginia

The College of William and Mary, Williamsburg, Virginia

Tohoku University and KEK, Tokyo, Japan *University of Regina, Canada*

Yerevan Physics Institute, Yerevan, Armenia

University of Georgia, Athens Georgia *INFN - Lecce, Italy*

INFN - Bari, Italy

June 3, 1998

Current:	Cryogenic Targets:	Beam Energies:	Beam Time:
75 μ A	LH2 15 cm	3.2, 3.6, 4.0, 4.8, 5.2, 6.0 GeV	520 hours

Abstract

This is a re-submission of the Conditionally Approved PR94-108. The experiment will measure exclusive kaon production cross sections in the $H(e,e'K^+)Y$ reaction. This experiment will measure how kaons are produced – the electromagnetic structure and which to what extent the various production mechanisms contribute. Three of the four unpolarized response functions will be separated over a large range in Q^2 , W , and t .

The longitudinal and transverse response functions will be separated through the detection of kaons along the direction of the virtual photon, where only these terms contribute to the cross section. For each Q^2 kinematic the longitudinal and transverse responses will be separated at three different points in t . By appropriately extrapolating the longitudinal term in t , the electromagnetic form factor of the kaon will be determined. The separation of the longitudinal-transverse interference term will also be performed for selected kinematics, forming a sensitive test of the production model. The t -dependence of the cross section (and additionally of the separated transverse response at small $|t|$) will also be measured to very large values of $|t|$, covering the transition from a semiphenomenological description in terms of mesons and baryons to a pQCD-based description in terms of quarks (or diquarks).

The square of the 4-momentum transferred by the electron will cover the range $2 \leq Q^2 \leq 3$ (GeV/c)², the hadronic 4-momentum transfer squared will cover the range $-0.3 \geq t \geq -3.0$ GeV², and the invariant mass will cover the range $1.8 \leq W \leq 2.2$ GeV. The measured cross sections will be compared to both hadronic and subnucleonic reaction models. This will considerably extend the present electroproduction data. Incident beam energies from 3.245 to 6.045 GeV will be utilized, along with the Hall A spectrometers. It should be emphasized that with 520 hours, this experiment will provide a consistent data set in a wide region of Q^2 , W , and t , which cannot be accessed elsewhere at CEBAF.

1 Introduction

1.1 Physics Motivation

The past five years have seen the first new data on electromagnetic kaon production.[1, 2] However the current situation for kaon photo- and electroproduction remains unsatisfactory, both from the experimental and theoretical point of view. Measurements of the $\gamma + p \rightarrow K^+ + Y$ and $e + p \rightarrow e' + K^+ + Y$ ($Y = \Lambda, \Sigma^0$) reactions have been limited by short lifetimes ($c \cdot t_K = 370$ cm, $c \cdot t_\Lambda = 8$ cm), small production rates (an order of magnitude smaller than for pions) and high thresholds [$E_{th}(K\Lambda) = 911$ MeV, $E_{th}(K\Sigma^0) = 1.05$ GeV]. Knowledge from photoproduction data (reviewed, e.g., in ref. [3, 4]) has not improved much in twentyfive years. The unseparated cross sections are known with an accuracy of about 10%. The single polarization asymmetries are only recently determined and only for a few points, all in Λ production with errors of 25% to 50%. The photon energy range is limited to $0.9 \leq E_\gamma \leq 1.4$ GeV (a few additional points were measured [5, 1, 6] at a fixed momentum transfer $t = -0.147$ GeV² in the energy range $E_\gamma = 1.05 - 2.2$ GeV).

Λ -electroproduction data are more sparse[2, 7, 8, 9] with only one actual structure function separation.[2] The experimental information on Σ^0 production is even more scarce. In the following we will focus on the Λ production, but all proposed measurements on the proton will also allow simultaneous measurement of the Σ^0 channel (with reduced statistics).

There are also theoretical problems in understanding the electroproduction process. In the low energy region various semiphenomenological descriptions in terms of mesons and baryons have been used. The hadronic field theories do not explicitly contain the quark degrees of freedom, but provide an effective description of the dynamics in the low- and intermediate-energy range. The semiphenomenological parameters of the theory (strong coupling constants, transition magnetic moments) are fit to the available photoproduction data using transition amplitudes based on the tree level Feynman diagrams.

In general, phenomenological χ^2 parameter fits are not unique due to the large number of coupling constants (up to 12 effective parameters are used; four of them enter the Born terms and the rest are associated with the resonance terms[10]) and the experimental uncertainties and limited kinematical region that has been so far explored. Hence, many sets of the parameters can fit the data equally well in the photoproduction channel. The various fits, however, differ when extrapolated outside the kinematics used in the fitting procedure ($E_\gamma \geq 1.4$ GeV, virtual photons). The fits are also not equivalent from the point of view of the theoretical interpretation.

First is the disagreement between the values of coupling constants derived from the purely hadronic processes and from the available photoproduction data. The value of the leading coupling constant $g_{K\Lambda p}/\sqrt{4\pi}$ is in the range from -1 to -3 in most photoproduction models, while its accepted hadronic value is about -4[11], in agreement with the broken SU(3) prediction[4]. This discrepancy can be resolved by inclusion of the t-channel K_1 resonance state with $J = 1^+$ (M=1280 MeV, $\Gamma=90$ MeV) but only at the price of a very strong $K_1\Lambda p$ coupling[3, 4].

Thus, the situation in the theory of photo- and electroproduction of strange mesons is rather complicated. A variety of models (see e.g. review in [3]) differing in contributing resonances and coupling constants (including the leading ones $g_{K\Lambda p}$ and $g_{K\Sigma p}$) fit the available photoproduction data equally well - Figure 1[3].

The Λ polarization data are more selective in this respect. Here predictions of various models differ significantly; nevertheless, only the models based on the Born diagrams alone can be

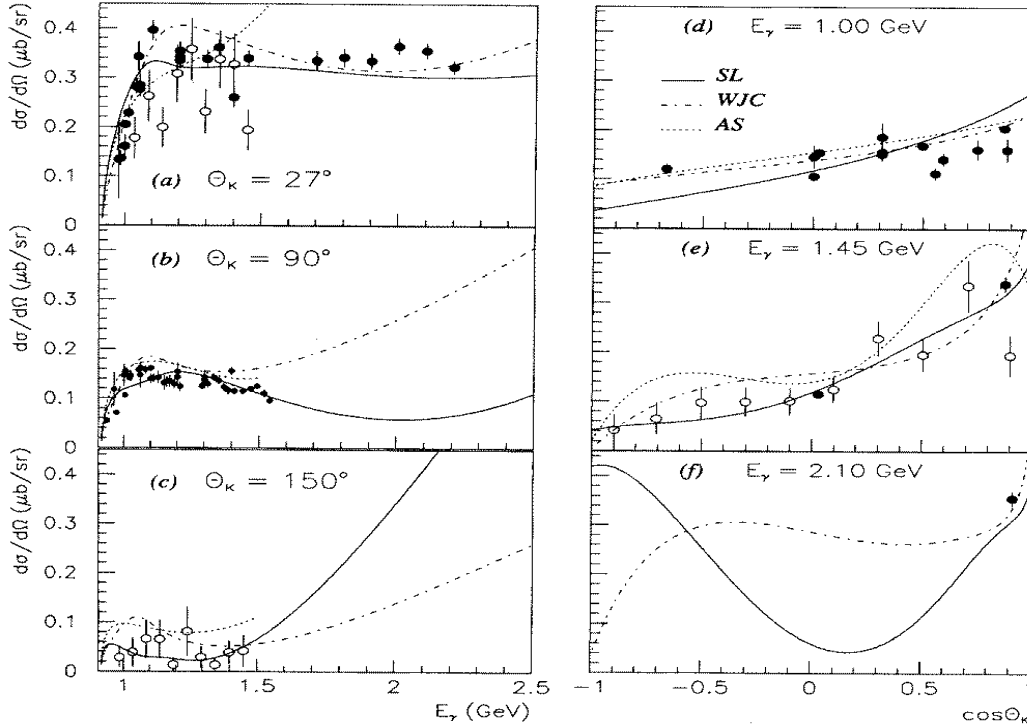


Figure 1: The photoproduction cross section calculated with different coupling constants.[3]

rejected.[12, 3]

Philosophically, with the construction of a high energy, high quality, high duty factor, and high intensity electron beam facility at CEBAF, it becomes possible and pertinent to investigate the properties of quarks inside a nucleon in an exclusive (e,e'q) experiment similar to the (e,e'p) or the (p,2p) studies for nucleons inside a nucleus.[13] Such an exclusive measurement samples (*i.e.*, isolates) a specific channel of the deep inelastic inclusive cross section. However, before the struck quark reaches the detector, it turns itself into color singlet hadrons. Study of the properties of the hadron system produced following the deep inelastic scattering may give information on the mechanisms by which the nucleon's partons rearrange themselves into the observable hadrons after the primary scattering. These mechanisms must be related to the forces that bind partons into the original nucleon, and may shed insight as to why no parton has yet been observed as a separate entity.

Due to the lack of data, attempts to investigate the problem of electromagnetic production of strangeness on a subnucleon (quark) level are only beginning. Only recently has the photo- and electroproduction reaction been calculated in terms of the hard scattering model of Brodsky and Lepage[14, 25], and of the diquark mechanism[15].

The electroproduction of kaons at CEBAF energies may also give insight about the transition to quark degrees of freedom: In a naive quark-parton model, and assuming the string fragmentation model, the production of a K^+ can be considered to occur in two steps. First, a u quark is struck. As the u quark moves away from the target remnants, the color string between the u quark and the remnants breaks, producing an $s\bar{s}$ quark pair. If there is additional energy stored in the color strings, more $q\bar{q}$ pairs will result producing more hadrons. Because of the "low" energy in the

CEBAF beam and the “high” masses of the kaon and the hyperon which are produced, the particle multiplicity will usually be low (as opposed to, say, pion electroproduction). For those events with only two particles in the final state (a kaon and a hyperon such as the K^+ and Λ for example), the transverse momentum of the produced kaon with respect to the 3-momentum transfer should be equal to the transverse momentum of the struck quark, or the primordial k_T . In this sense the dynamics of the struck quark are “preserved.” As the incident electron energy increases beyond the range available at CEBAF, the particle multiplicity will also increase, meaning the K^+ and Λ would only be part of the jet fragments.

1.2 PAC Concerns

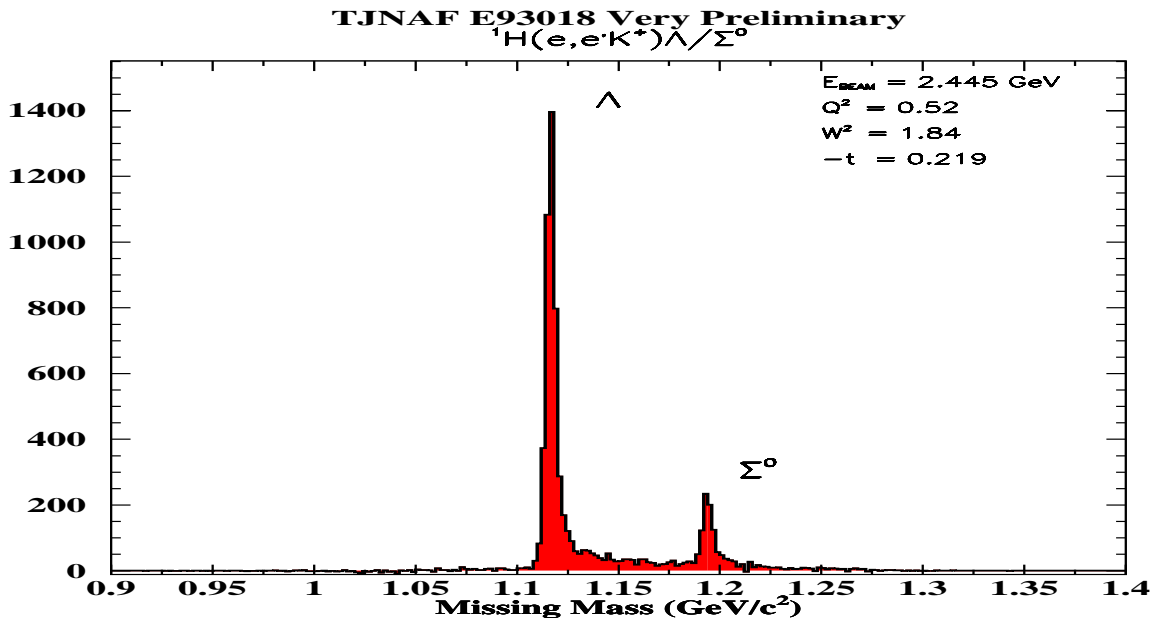


Figure 2: The missing mass spectrum from the Hall C experiment.

The PAC gave the experiment conditional approval contingent on a realistic assessment of the Hall A errors and a successful demonstration of the L/T separation in Hall C. The goal of the systematic errors was 2% overall. PAC-9 wrote “the goal of achieving 2% systematic error is ambitious”. We have backed off from this, and are now aiming for only 2.8% point-to-point and 4.4% overall scale systematic errors, as listed in Tables 10, 11. At the same time, by enlarging the lever arm in ε , we have REDUCED the error in the longitudinal cross section (as compared to our earlier proposal) by the choice of beam energies.

We discuss the progress made on the systematic errors in Section 4.3 of this proposal. We have included a parameterization of the cross section into MCEEP to estimate the effects of the systematics on the response function separation. The PAC also questioned the particle identification, particularly for K^+/p separation. We have monte carloed the particle identification, and demonstrate in section 4.1 that we can meet the requirements of this experiment.

The Hall C experiment[2] has now been analyzed and shows: Firstly, clean particle identification is achieved with a setup similar to what will be used in Hall A (we will be at higher energies and

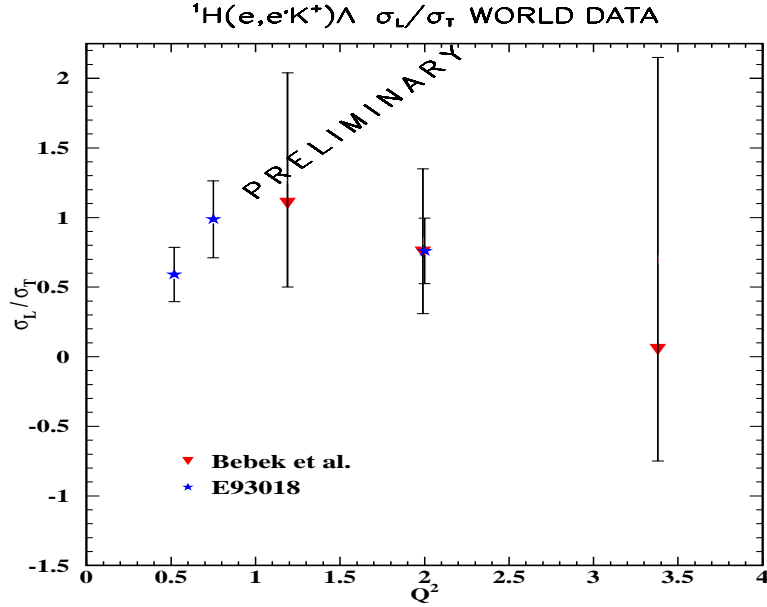


Figure 3: The ratio of the longitudinal-to-transverse from the Hall C experiment. (c) Gabriel Niculescu 23/10/97

therefore will use a slightly different index aerogel) as in Figure 2[2]. The Λ and Σ^0 peaks are cleanly separated and have essentially no background under them. Second, that the longitudinal contribution to the cross section IS in fact large as in Figure 3. Plotted is the ratio of the longitudinal to transverse cross sections, versus Q^2 . Also shown is the previous attempt to do such a separation. Finally, Figure 4 shows that the L/T separation can be accurately done. Plotted is the reduced cross section versus the virtual photon polarization. The intercept gives the transverse part of the cross section and the slope gives the longitudinal part. [Note that the scale in the vertical direction does not extend down to zero.]

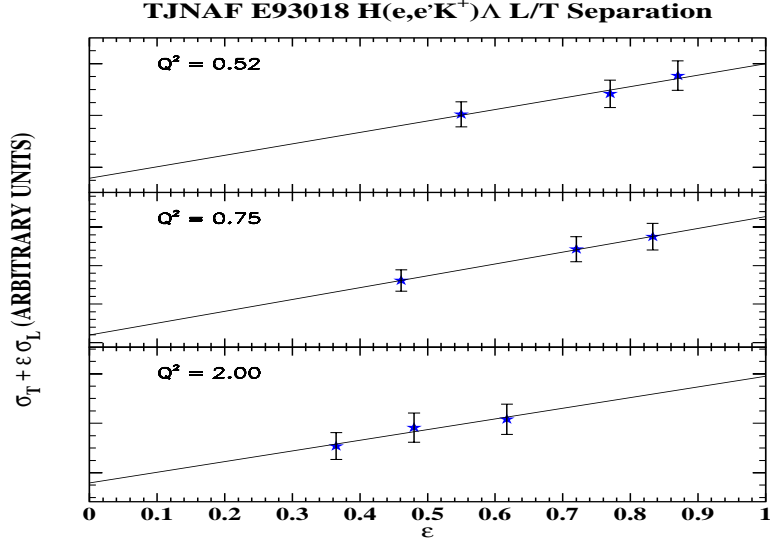


Figure 4: The reduced cross section versus ϵ .

1.3 Measurements

The proposed experiment can be divided in three parts:

i) The separation of the longitudinal and transverse response functions through the detection of high momentum kaons along the direction of the virtual photon. For every Q^2 kinematic, three central settings in t (and W) will be measured. [The data can be more finely binned in t within the acceptance of the spectrometers.] The main goal of this part is the determination of the electromagnetic form factor of the kaon up to $Q^2 = 3.0 \text{ (GeV/c)}^2$ from the t -dependence of the longitudinal term.

ii) The separation of the longitudinal-transverse interference term which, in a quark model description, gives information on the magnitude of the transverse momentum of quarks. In hadrodynamic models, this observable has been shown to be extremely model sensitive, different models (and coupling constants) giving not only different magnitudes but the opposite sign in the observable.

iii) The t -dependence of the full cross section up to large values of $|t|$ where the transition from a semiphenomenological description in terms of mesons and baryons to a regime in which the theoretical approach based on quarks or diquarks description of the elementary process is applicable. [We also have the t -dependence of the transverse part of the cross section at lower $|t|$. The models which incorporate some form of a kaon pole indicate that as we increase $|t|$ the cross section should become transverse.]

The experiment will provide a considerable set of data over a large kinematical region in W , Q^2 , and t , placing severe constraints on the models used to reproduce the data. In particular, important parameters such as the $g_{K\Lambda p}$ coupling constant used in semiphenomenological models based upon hadron dynamic (QHD) formalism, can be much better established. Additionally the transition region to a more fundamental description of the reaction in terms of quarks can be identified, as well as determining which among the various proposed “pure quark” or “diquark” models has better reproducibility.

1.4 Comparison to Other Experiments

The accuracy of the HRS2 spectrometers in Hall A is ideal for these measurements since systematic uncertainties are magnified in the extraction of the response functions. More specifically, good angular resolution is required to accurately extract small amplitudes; the angular resolution and momentum resolution both enable the accurate kinematics binning event-by-event. The spectrometer acceptances are flat to allow good binning of the data as a function of t . The HRS angular resolutions have been shown to be better than 2 mr in the horizontal (scattering) direction and 6 mr in the vertical direction.

The long flight path of the HRS2 means that the kaon survival fraction ranges between 14–36% for our kinematics, but the same flight path is responsible for the success of the time-of-flight particle identification. The missing mass resolution of the HRS2 will also cleanly separate Λ , Σ^0 final states from the continuum or higher resonances.

The experiment can only be carried out in Hall A. Hall B, while tempting because it would enable one to take a large volume of phase space in one bite, does not have the particle identification capability at high momenta required by this experiment (in the CLAS identifying kaons with momenta $\geq 2.0 \text{ GeV/c}$ is challenging). This experiment, while mapping out a large area of

phase space not previously measured, also concentrates on high momentum, high invariant mass, and minimum $|t|$ (i.e., the kaon-virtual photon angle=0), thereby focussing the kinematics on (relatively) forward scattering angles. This means that the large solid angle afforded by the CLAS does not help much. Moreover, to do an L/T separation, a large number of statistics is required in a very small kinematics bin, making Hall B a poor choice. However Hall B is still the best place to separate the fourth unpolarized response function, as well as map out the general trends of the data with W . This will be focus of two Hall B proposals, one on photoproduction –obviously an L/T separation is not possible, and the other on electroproduction although at lower energies similar to what has just been done in Hall C.[21, 20] The Hall A experiment is at higher energies, but is basically complementary (not competitive) to these Hall B proposals.

Hall C has recently completed two very successful experiments.[22, 23] Because of the high kaon and electron momenta, the SOS in Hall C is not suitable for this experiment. [Even switching the SOS to the electron arm and the HMS to the Kaon arm would not work since both arms need high energies to do the separation.] The physics here extends the kinematics. Hall C has clearly demonstrated that the most exciting results come from the higher Q^2 where tighter constraints can be put on the models as well as the baryon electromagnetic form factors.

Hall A has a complementary experiment submitted to this PAC to measure the Λ polarization in photoproduction ($\gamma p \rightarrow K^+ \Lambda$) to try and understand the reaction mechanism involved. This is a different (complementary) technique. The energies are also slightly higher (using 3-6 GeV photons), but the PID issues are related. There is overlap among the collaborations.

The remainder of the proposal is split as follows: Section 2 defines the kinematic variables, discusses the hadronic and quark models for the cross section, estimates the behavior of the cross section as a function of Q^2 , W , and t , and provides physics details on the experiment goals. Section 3 lists the kinematics, rate estimates, cross sections and run times. Section 4 describes the particle identification and error analysis, and Section 5 summarizes the beamtime request and gives the experimental runplan.

2 Observables, Physics Models and Experiment Goals

2.1 Kinematical Variables and the Cross Section

The definitions of the kinematical variables are given for the reaction $e + N \rightarrow e' + K + X$. The five 4-momenta involved are:

$$\begin{aligned} e &= (E, \vec{e}) \text{ for the incident electron} \\ e' &= (E', \vec{e}') \text{ for the scattered electron} \\ N &= (M, \vec{0}) \text{ for the target nucleon} \\ K &= (E_K, \vec{k}) \text{ for the produced kaon} \\ X &= (E_X, \vec{x}) \text{ for the unobserved residual system.} \end{aligned}$$

A few Lorentz invariants and other kinematic variables are defined below as:

$$\begin{aligned} \gamma_v^2 &= (e - e')^2 = -Q^2 \\ \nu &= E - E' \\ \epsilon &= [1 + 2\frac{\nu^2 + Q^2}{Q^2} \tan^2 \frac{\theta_e}{2}]^{-1} \\ \epsilon_L &= \frac{Q^2}{\omega^2} \epsilon \\ s &= (\gamma_v + N)^2 = W^2 \\ t &= (\gamma_v - K)^2 \\ x_B &= Q^2 / 2M\nu \\ y &= \nu / E \\ z &= E_K / \nu \\ M_X^2 &= (e - e' + N - K)^2 \end{aligned}$$

The differential cross section can be expressed as:

$$\frac{d^3\sigma}{dE'd\Omega_{e'}d\Omega_K} = \Gamma \cdot \frac{d\sigma_v}{d\Omega_k}$$

Γ is the virtual photon flux, given by:

$$\Gamma = \frac{\alpha}{2\pi^2} \frac{E'}{E} \frac{s - M^2}{2MQ^2} \frac{1}{1 - \epsilon}$$

The cross section for single kaon production by virtual photons is given by

$$\frac{d\sigma_v}{d\Omega_k} = \frac{d\sigma_T}{d\Omega_k} + \epsilon_L \cdot \frac{d\sigma_L}{d\Omega_k} + \epsilon \cdot \frac{d\sigma_{TT}}{d\Omega_k} \cdot \cos(2\phi) + \sqrt{2\epsilon_L(\epsilon + 1)} \cdot \frac{d\sigma_{LT}}{d\Omega_k} \cdot \cos\phi$$

where ϕ is the angle between the kaon production plane and the electron scattering plane, and ϵ is the virtual photon polarization parameter. The pieces correspond to the cross section for unpolarized transverse (σ_T), longitudinally polarized (σ_L), polarized transverse interference (σ_{TT}), and polarized longitudinal-transverse interference (σ_{LT}) kaon production by virtual photons and only depend on the variables Q^2 , s , and t . In order to separate all four pieces of the cross section (σ_T , σ_L , σ_{TT} , and σ_{LT}), a spectrometer with out-of-plane detection capability is needed to determine the ϕ dependence of the cross section. For the special case in which the kaon is detected along the direction of the virtual photon, the interference terms vanish and σ_L and σ_T can be separated using a minimum of two measurements at different values of the virtual photon polarization ϵ .

2.2 Description and Analysis of the Models

In order to have clear information on the electroproduction process, a comprehensive data set of cross sections and the extracted response functions are needed over a large range of W , Q^2 and t . The kinematic region of this experiment covers a transition between “traditional” nuclear physics and the deep inelastic region. There are several competing pictures of the reaction. Two extreme approaches are used here to provide guidance: semiphenomenological hadrodynamical scattering and quark hadronization. Seeing whether the data can be reconciled with any of the models is one goal of the experiment. Although obtaining data at very small x_B would provide the most information on the quark momentum distribution, the SLAC data[18] show that quark degrees of freedom evidence themselves at values of Q^2 as low as 1 (GeV/c)².

The hadronic field theories (e.g., the quantum hadrodynamics QHD) do not explicitly contain the quark degrees of freedom, but they provide a suitable effective scheme for description of dynamics in a low and intermediate energy range. The QHD is properly relativistic and simply related to the covariant S-matrix formalism. The semiphenomenological parameters of the theory (such as the strong coupling constants and transition magnetic moments) are fitted to the available data, making use of the transition amplitudes based on the tree level Feynmann diagrams (figure 5).

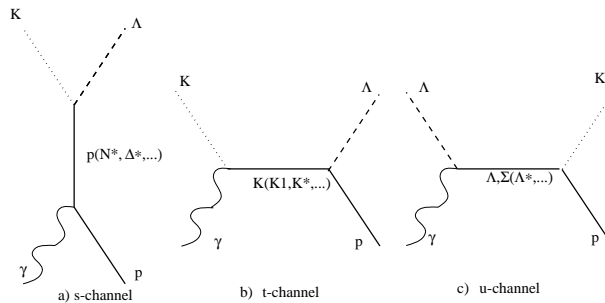


Figure 5: Tree level Feynman diagrams in kaon electroproduction.

In the intermediate state the particles which can be present are: in the s-channel a proton (Born term) or other strangeless nucleon resonances (figure 5a); in the t-channel the K^+ (Born) or kaon resonances (figure 5b); in the u-channel the hyperons Λ or Σ (Born) or other spin 1/2 hyperons (figure 5c).

A variety of models were examined which used such a diagrammatic approach; the differences being mainly different particles in the intermediate state and the values of coupling constants and transition magnetic moments. The parameters used for all the models result from fitting to the available photoproduction data (a few also include electroproduction data). A general code considered more than ten models[12] varying intermediate particles, coupling constants and transition moments, as well as different form factors. Beyond reproducing the cross sections provided by the authors of the models, further analysis compared predictions for the exclusive electroproduction reaction in the channel K - Λ extending the kinematical region (out from the region where the model was fit to the data). The results show that the data is reproduced very well by two of the considered models (referred to as wjc2 and wjc4 coming from the parameters set II from [28] and [10] respectively). While wjc4 is more complete from the theoretical point of view and has a good reproducibility for different reaction channels (namely $p(e,e'K)\Lambda$, $p(e,e'K)\Sigma$ and $p(e,e'K)\Lambda(1405)$, model wjc2 more accurately reproduces the measured cross section in the exclusive channel $p(e,e'K)\Lambda$. For

example, the existing data up to about $Q^2 = 4 \text{ (GeV/c)}^2$ [29] are reproduced by the model wjc2 while they are significantly underestimated at high Q^2 by wjc4. In addition, the K - Λ data reported in [10] (where the wjc4 model is presented) are well described by wjc2 as well and, moreover, the t -dependence of the cross section is in better agreement with the data which suggest a decrease in the cross section with increasing $|t|$, as suggested by photoproduction data (and almost all the models considered). Finally, σ_{LT} and σ_{TT} data[7] are better reproduced by wjc2 than wjc4. The latter predicts rather large contributions of the interference terms not suggested by the data. Nevertheless, when compared to the poor accuracy of existing electroproduction data, both models can be considered consistent with the existing data even if for high Q^2 wjc2 appears preferable.

Some of the models we have considered also include crossing (as do both wjc2 and wjc4) and duality (also included in wjc4). The crossing constraint relates reactions with particles in the initial or final state with reactions with antiparticles in the final or initial state (and vice versa) thus making crossing a symmetry of the S matrix. The duality constraint, based on the dual role of resonances in the s (u) and t channel, is used to restrict the number of resonances considered in the intermediate states, resulting in a model which includes only the s and u -channel resonances along with the usual Born terms (including the K^+ exchange in the t -channel required by gauge invariance).

2.3 The Kaon form factor

The separation of as many of the response functions as possible is essential in differentiating between hadronic and quark degrees of freedom. In the quark picture, the interaction with the virtual photons contributes mainly to the transverse cross section (see the discussion below). On the other hand, an enhancement of the longitudinal cross section at small t (the squared 4-momentum transfer to the unobserved residual system) could indicate the influence of quasifree scattering from the kaon, as has been seen in pion electroproduction. As in the case of the pion, the Q^2 dependence of σ_L can then be used to determine the kaon form factor.[23, 34]

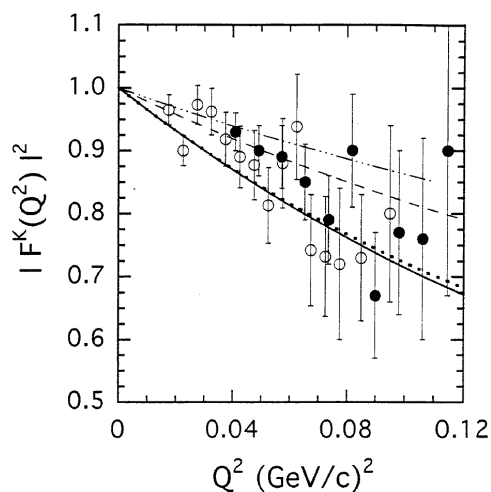


Figure 6: The Kaon form factor, $F_K(Q^2)$, plotted as a function of Q^2 .

The knowledge of the electromagnetic structure of any complex particle, made of charged sub-structures, always has been essential in the comprehension of its structure in terms of the behaviour of the more fundamental components. The electromagnetic form factor can be theoretically deduced from models describing the way elementary components aggregate to form complex structures. It depends only on the square of the four-momentum transfer to the particle by the electromagnetic probe. Electron-positron colliding beam experiments measure the form factor in the time-like region, generally via the production of a particle-antiparticle pair. The measurement of the form factor in the space-like region is straightforward for nucleons or nuclei as they can be used as free targets; only in these cases are the cross sections directly proportional to the absolute square of the form factor.

Particles (mesons and baryons) that can be produced in sufficient quantity to be used as secondary beams in large hadron accelerators can be scattered from atomic electrons to measure the form factor, but due to the small electron mass only low values of momentum transfer can be obtained. At large space-like momentum transfers, the only reaction that can give information on form factors is the electroproduction process. The extraction of the kaon form factor from the data requires effort both on the experimental and theoretical side, as in the case of the pion form factor[29, 35].

The existing measurements in the space-like region come from K - e scattering [29, 36] and are limited to a maximum Q^2 of 0.1 (GeV/c)^2 . Figure 6 shows this data, along with a recent theoretical calculation[37]. Determining the kaon form factor through the electroproduction reaction relies on two things. First that the t diagram of Figure 5 has the kaon as the meson exchanged (kaon pole diagram), and that this kaon exchange dominates all the other diagrams near the unphysical value $t = M_K^2$. Second it relies on this behaviour being strong enough at physical values of t to allow a smooth extrapolation from experimental points to $t = M_K^2$. Theoretical guidance is necessary in the extrapolation to exploit model-independent constraints and analytical properties of the amplitudes. Experimentally, precise measurements are required in kinematical conditions favourable for the extrapolation (reaching as low as possible in $|t|$ approaching the unphysical region). For a given Q^2 and a given W there is a minimum value for the variable t in the physical region (t_{min}) that corresponds to the kinematical condition in which the kaon is emitted in the same direction as the 3-momentum transfer. In Figure 7 the dependence of t_{min} on W for different values of Q^2 is shown. We want to measure the longitudinal and transverse response functions with a Rosenbluth separation at three values of Q^2 : 2, 2.5 and 3 $(\text{GeV/c})^2$ and a range of values of t for every Q^2 measurement. In these measurements W varies between 1.8 and 2.2 GeV.

The models assume a form for the dependence on the invariant mass W . This experiment will determine the dependence of the separated response functions on W , providing the theoretical models with an additional constraint. Extracting the kaon form factor from the longitudinal response function is model dependent; extrapolation of the longitudinal response function in t is somewhat less so. If the data can be described by the model then it gives some confidence that the coupling constants are correctly known. The success (or failure) of the model to describe the data can be attributed in large degree to the knowledge of these coupling constants.

The kaon form factor is proportional to the square root of the longitudinal response function extrapolated to the kaon pole[35]:

$$F_K^2(Q^2) = F_K^2(Q^2, t)|_{t \rightarrow M_K^2} = \frac{(t - M_K^2)^2 \sigma_L}{N(t)}|_{t \rightarrow M_K^2}$$

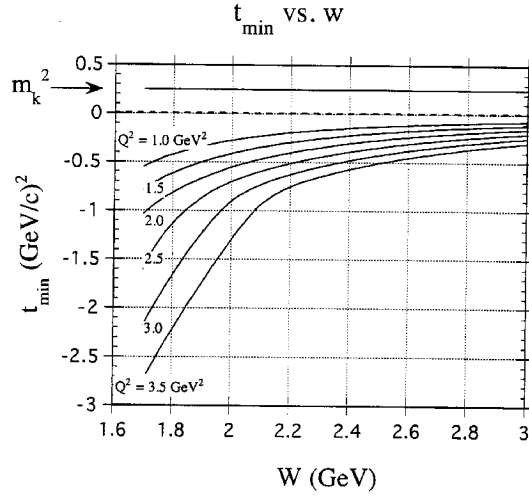


Figure 7: Loci of the minimum $|t|$ reachable for a given W and Q^2 . Each curve refers to a constant Q^2 value shown in the figure.

where

$$N(t) = (-t)8cg_{KNY}^2[k^2 \sin^2 \theta_e \frac{1 + \epsilon \cos 2\phi}{2} + \epsilon \frac{(qE_K - \nu k \cos \theta_e)^2}{Q^2}]$$

According to some nuclear interaction models, the kaon form factor has been shown to dominate the longitudinal response function at the kaon pole.[10] Assuming the kaon pole does dominate the cross section for small $|t|$, then the kaon form factor can in principle be determined (if the coupling constants are also known).

Figure 8 shows the kaon form factor $Q^2 F_K(Q^2)$, as a function of Q^2 , [37] in the region to be explored in the present experiment. Our actual experimental error bars will be 2-3 times smaller than the errors assumed here meaning the kaon form factor will also have correspondingly smaller error bars. Also shown are other simpler Vector Mesons Dominance Model predictions which consider, the ϕ - and ρ -mesons and predictions from the only available model based on a more fundamental microscopic approach[37]. Due to the model dependence and the extrapolation to the kaon pole, a prior analysis of the theoretical uncertainties in the kaon form factor is difficult. To illustrate, the extracted ratio $(t - M_K^2)^2 \sigma_L / N(t)$ for two models has been extrapolated in t at $Q^2 = 1.5 \text{ (GeV/c)}^2$ and $\langle W \rangle = 2 \text{ GeV}$. Figure 9 shows the t -dependence (along with the projected uncertainties) according to model wjc2, along with the kaon form factor extrapolated to the pole ($t = M_K^2$). As can be seen the longitudinal term is fairly flat and below the “correct” value of the squared form factor; *i.e.*, the kaon-pole diagram does not dominate at small $|t|$ approaching the unphysical region.

The situation is better if the analysis is done in the wjc4 model. In this case, as can be seen in figure 10, the kaon pole diagram dominates approaching the positive- t region. A simple extrapolation obtains a reasonable value of the kaon form factor with a reasonable uncertainty (being half that of the SQUARED extrapolated form factor). The two extrapolations are differentiated only by modelling the data in the physical region; further these are not extreme cases, meaning that we also have analysed models more and less difficult to extrapolate.

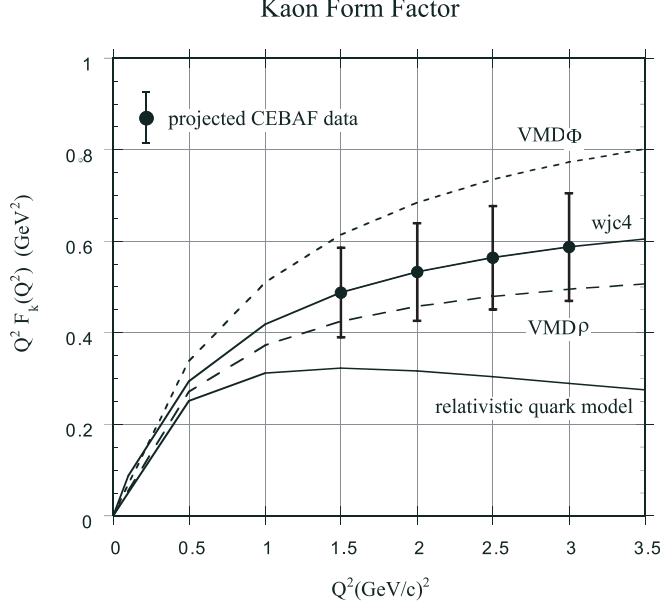


Figure 8: $Q^2 F_K$ versus Q^2 . The actual error bars will be smaller than the ones shown here. Only the points at $Q^2=2.0, 2.5$, and 3.0 will be measured.

2.4 Transverse Momentum of the Quark

Measurement of σ_{LT} will shed light on the processes which contribute to the interference cross section, as well as give information on the magnitude of the “apparent” transverse momentum of quarks which could result from effects such as the primordial transverse momentum, the initial and/or final state soft gluon radiations, and the initial and/or final parton showers. $\langle \cos \phi \rangle$ is measured by subtracting measurements made left of the direction of the virtual photon ($\phi = 180$) from measurements made right of the virtual photon ($\phi = 0$), at the same Q^2 , W , and t . $\langle \cos \phi \rangle$ is defined as:

$$\langle \cos \phi \rangle = \frac{\frac{d\sigma_v(\phi=0)}{d\Omega_K} - \frac{d\sigma_v(\phi=180)}{d\Omega_K}}{\frac{d\sigma_v(\phi=0)}{d\Omega_K} + \frac{d\sigma_v(\phi=180)}{d\Omega_K}}$$

If an electron scatters relativistically off a pointlike target, because of the helicity conservation, either (i) $\sigma_T = 0$ and $\sigma_L \neq 0$ if the pointlike target has spin 0, meaning $R = \frac{\sigma_L}{\sigma_T} \rightarrow \infty$, or (ii) $\sigma_T \neq 0$ and $\sigma_L = 0$ if the pointlike target has spin 1/2, or $R = \frac{\sigma_L}{\sigma_T} \rightarrow 0$. A small experimental value of R in the DIS region suggests that the longitudinal cross section is nonzero. Two possible sources for the longitudinal amplitudes are: (i) the initial (primordial) transverse momentum of the struck quark, and (ii) the higher-twist correction to the quark-parton model. The former is a pure kinematic effect and was predicted to give a negative contribution to the longitudinal-transverse (LT) interference asymmetry as:[38]

$$\langle \cos \phi \rangle \sim - \frac{(2k_T/Q) \cdot (2-y) \cdot (1-y)^{1/2}}{[1 + (1-y)^2]}.$$

The latter is a dynamic effect and was first predicted to give a positive contribution to the LT

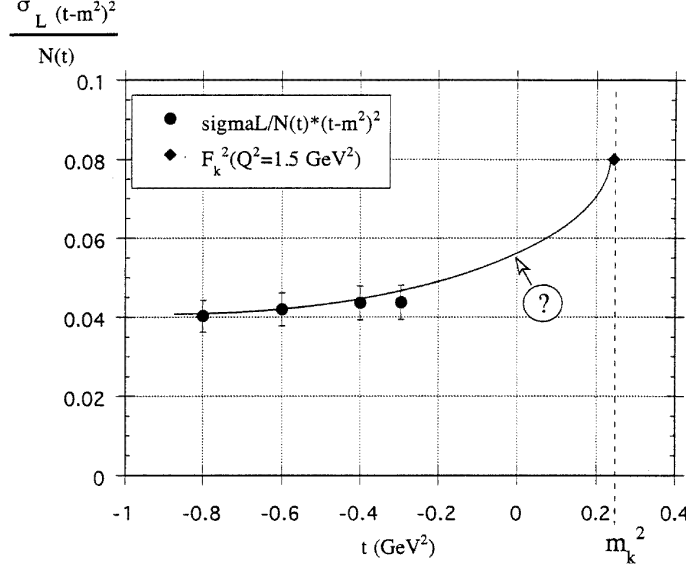


Figure 9: The t -dependence (along with the projected uncertainties) according to model wjc2, of the kaon form factor extrapolated to the pole ($t = M_K^2$).

interference cross section as:[39]

$$\langle \cos \phi \rangle \sim (k_T/Q) \cdot (1-y)^{1/2}$$

More recently, realistic quark wavefunctions have been included which give the prediction of the behavior going as:[40]

$$\langle \cos \phi \rangle \sim 1/2(k_T/Q) \cdot \frac{(2-y)\sqrt{1-y}H_3}{x_B y^2 H_1 + (1-y)H_2}$$

Plotted in Figure 11 is the longitudinal-to-transverse interference asymmetry, $\langle \cos \phi \rangle$ plotted as a function of z , the fraction of the energy transfer which ended up in the kaon.[40] Although the model uses more realistic quark wave functions, no intrinsic transverse momentum for the meson constituents is introduced. By prescaling pion data as well, the importance of the meson intrinsic transverse momentum can be estimated.

More conventionally, the LT -interference response function is a sensitive test of the various QHD models as well. Plotted in Figure 12 is the LT -interference response function versus Q^2 . The heavy solid line is the model of wjc2, the dotted line is the model of wjc4, and the dot-dashed line is the model W2 described earlier. The long-dashed line labeled TH1 is a model due to Thom. What can be clearly seen is that various models all differ widely in magnitude, sign and behavior. This makes the LT -interference an ideal tool to constrain the models before extrapolating to the kaon pole.

2.5 Tests of pQCD, large $|t|$ kinematics

The study of exclusive reactions at large $|t|$ provides a way to shed light on the interaction mechanism which occurs at short distances in hadronic matter, selecting a hard scattering regime of the reaction (in comparison with a diffractive mechanism that occurs at small $|t|$ values). Recently theoretical

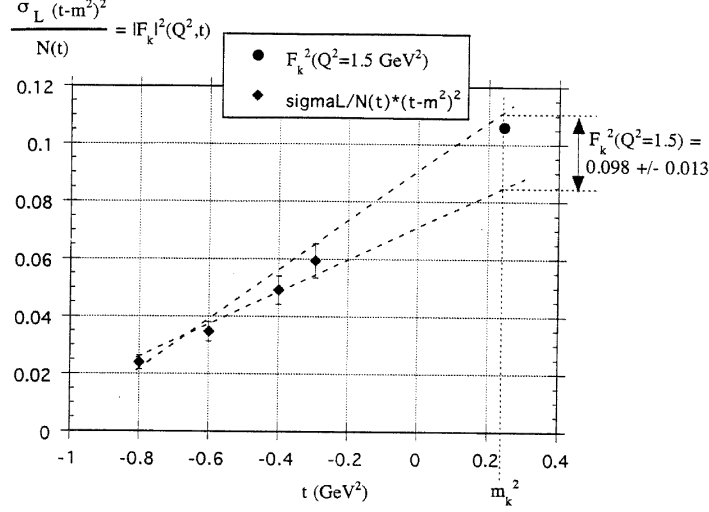


Figure 10: The t -dependence (along with the projected uncertainties) according to model wjc4, of the kaon form factor extrapolated to the pole ($t = M_K^2$).

predictions of exclusive photo- and electro-production reactions based on perturbative QCD[14] or on a QCD semiphenomenological diquark model have become available[15].

The kinematical region in which computations based on the diquark approach are applicable is within CEBAF capabilities [24] ($W \geq 2$ GeV) and this experiment will measure the angular distribution to values of $|t| \leq 3.0$ (GeV/c) 2 , covering the transition between small and large $|t|$ where different descriptions of the reaction should be applicable. Separating the response functions (at small $|t|$) and measuring the full cross section at large values of $|t|$ will provide more observables to compare with the theory and to give guidance if a discrepancy is found.

In the region where non perturbative effects are still present, an approach based on the idea of diquarks is both appropriate and promising. Recently, such theoretical predictions of exclusive photo- and electro-production of kaons based on QCD semiphenomenological diquark models have become available [25]

The main ingredients of the diquark model are: *i*) the baryon is treated as a quark-diquark system; *ii*) the use of phenomenological diquark form factors to take into account the composite nature of diquarks; *iii*) the gluon and photon couplings to diquarks.

In its ground state a diquark has positive parity and may be an axial-vector (spin 1) or a scalar (spin 0) boson. The baryon wave function can be written as

$$\Psi^B(p, \lambda) = f_S \Phi_S^B(x_1) \chi_S^B u(p, \lambda) + f_V \Phi_V^B(x_1) \chi_V^B \frac{1}{\sqrt{3}} (\gamma^\alpha + p^\alpha/m_B) \gamma_5 u(p, \lambda) \quad (1)$$

where the two terms represent configurations consisting of a quark and either a scalar (subscript S) or vector (subscript V) diquark and:

- i*) Φ^B are the baryon distribution amplitudes, the valence Fock-state (consisting of a quark and a diquark) wave functions integrated over the transverse momentum. The argument x_1 is the momentum fraction of the parent baryon carried by the quark ($p_q = x_1 p_B$). It is assumed

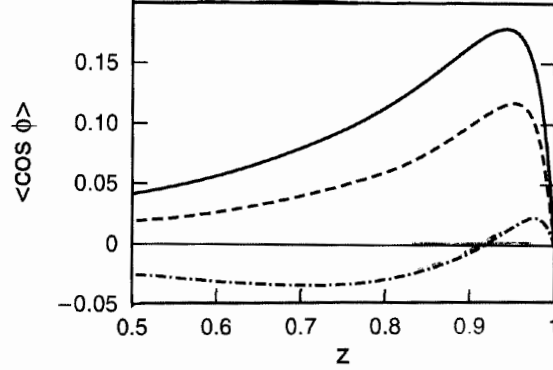


Figure 11: The asymmetry $\langle \cos \phi \rangle$ vs. z for $Q = 2.5$ GeV, $p_T = 0.5$ and $k_T = 0$ (solid line), 0.25 (dashed line) and 0.5 (dash-dotted line).

(collinear approximation) that it sums up to 1 with the momentum fraction of the diquark ($p_D = x_2 p_B = (1 - x_1) p_B$)

ii) f are the $r = 0$ values of the distribution amplitudes

iii) χ are the flavor functions and $u(p, \lambda)$ are spinors with helicity λ .

Investigating the $\gamma_V + p \rightarrow K^+ + \Lambda$ reaction, the hard scattering amplitude can be calculated perturbatively taking into account all the possible tree diagrams contributing to the elementary scattering process $\gamma u D \rightarrow u \bar{s} s D$ where D is a u - d diquark. In figure 13, only a few diagrams are reported as an example, together with a blob representation of the process.

The flavor functions $\chi_{S,V}^{p,\Lambda}$ for the proton and the lambda hyperon take on the form :

$$\chi_S^p = u S_{[u,d]} \quad , \quad \chi_V^p = [u V_{\{u,d\}} - \sqrt{2} d V_{\{u,u\}}] \quad (2)$$

$$\chi_S^\Lambda = [u S_{[d,s]} - d S_{[u,s]} - 2s S_{[u,d]}] / \sqrt{6} \quad , \quad \chi_V^\Lambda = [u V_{\{d,s\}} - d V_{\{u,s\}}] / \sqrt{2} \quad (3)$$

The simplifying feature of the specific process under investigation is that only scalar diquarks contribute, since, from eqn. (4) and (5), only scalar diquarks $S_{[u,d]}$ are common to both the proton and the Λ (while for the exclusive channel $\gamma_V + p \rightarrow K^+ + \Sigma^0$ only the vector $V_{\{u,d\}}$ diquark contribute). As a consequence, the number of diagrams is reduced to “only” 63.

Figure 14 shows the available data near CEBAF energies (4 and 6 GeV photon energies) on the Λ and Σ^0 photoproduction reaction together with the predictions of the pQCD model. Plotted is the cross section scaled by s^7 versus the $\cos \theta_{\gamma K}$, the cosine of the opening angle between the kaon and the photon which is proportional to t . The data is from Reference [33]. The long-dashed curve (the lowest) is a “pure” quark[14] while the others are diquark-model predictions calculated with three different baryon Distribution Amplitudes[25]. The quark calculation[14] is a leading twist calculation, using the Born approximation. The scattering is sensitive to the quark wavefunctions

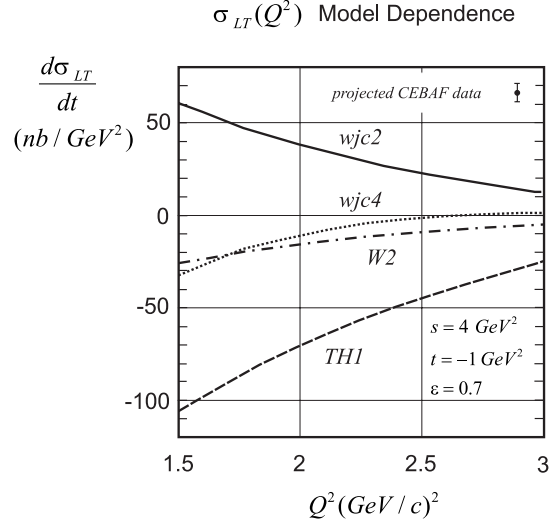


Figure 12: The LT -interference response function versus Q^2 .

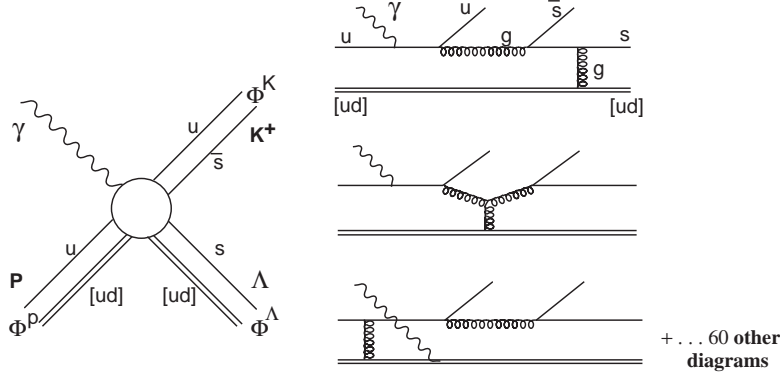


Figure 13: A few representative examples of diagrams contributing to the process $\gamma u[ud] \rightarrow u \bar{s} s[ud]$

and assumes the scattering is from the valence quarks. The model calculates the hard scattering in the s -channel with real photons. As can be seen, the data do not agree with the calculation. At the forward channels, the t -channel can contribute (and at backward angles from the u -channel can contribute).

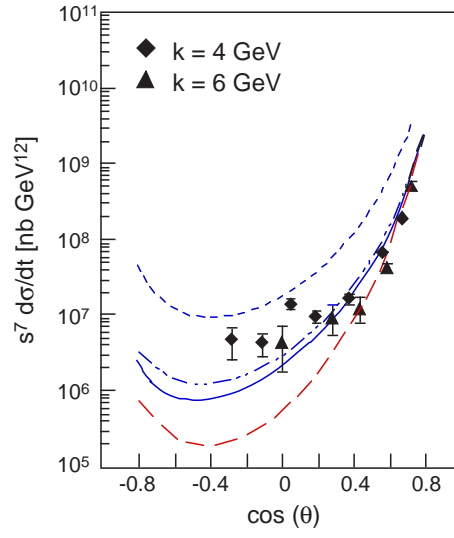


Figure 14: The a) $\gamma p \rightarrow K^+ \Lambda$ and b) $\gamma p \rightarrow K^+ \Sigma^0$ cross sections scaled by s^7 .

3 Kinematics, Count Rates and Runtimes

3.1 Kinematics

The kinematics for the longitudinal-transverse (L/T) separation are given in Table 1. The L/T separations require measuring the cross section at different values of ϵ , the virtual photon's polarization, while centering the hadron arm around θ_q , the angle of the virtual photon ($\theta_k = \theta_q$). In this manner the contributions from the interference terms (σ_{LT} and σ_{TT}) are averaged away. By performing the separations as a function of W , the invariant mass, and t , the hadronic momentum transfer, additional constraints will be put on the models which predict the kaon form factor. [The kaon form factor, extrapolated in t , should have only a Q^2 dependence, not a W or t dependence.] The range in ϵ , the polarization of the virtual photon, is not always as large as might be desired, the highest value limited by the 6 GeV beam and the lowest value limited by the minimum spectrometer angle (12.5 degrees). Energies of 3.6, 4.8 and 6.0 GeV were chosen as multiples of the 5-pass maximum energy. 3.245 and 4.045 GeV are standard 5-pass energies, making only 5.2 GeV a non-standard energy.

The longitudinal-transverse interference response function σ_{LT} will be extracted using the kinematics given in Table 2. The electron angle and momentum will be kept constant (fixing Q^2 and W) while the kaon is detected left and right of the virtual photon. By moving left and right symmetrically about the direction of the virtual photon, t was kept constant for this measurement. Subtracting the left and right measurements will separate σ_{LT} from the combination ($\sigma_T + \epsilon_L \sigma_L + \epsilon \sigma_{TT}$). Counting times were minimized by performing the measurements at the same electron settings as the forward angle point of the L/T separation.

The t -dependence for the unseparated cross section will be mapped out from $-3.0 \leq t \leq -0.3$ by changing the kaon angle and momenta, at a constant electron angle and momentum. Table 3 gives the kinematics for the t -dependence measurements. Again, counting times were minimized by performing the measurements with the electron arm at the forward angle point for the L/T separation (as it was for both the L/T separation and the σ_{LT} -interference measurement) and moving the kaon arm to larger angles, changing the angle between the kaon and the virtual photon. However it is no longer possible to measure both left and right of the direction of the virtual photon (as done for $\langle \cos \phi \rangle$) because the measurement would require a smaller spectrometer angle than the minimum available to access the “left” kinematics.

The models predict that the transverse part of the cross section dominates at large $|t|$, meaning that effectively σ_T is being measured. The L/T separations (plotted as a function of t) will test this hypothesis. The full cross section (as opposed to the individual response functions) will be measured in the hard scattering region.

3.2 Cross Section Estimates and Rates

Table 4 shows the singles and coincidence rates for the L/T separation. The electron single arm rates were computed using the Monte Carlo code XSECDEEP[41] based on the SLAC deep inelastic scattering data, and averaging over the spectrometer angular and momentum acceptances. The pion rates were determined by using PIXSEC,[42] which averaged the single arm pion cross section over the spectrometer acceptances. The code computes the point cross section based on a fit to deep inelastic (e, π^-) data taken at SLAC. The (e, π^+) rates were assumed to be the same as the (e, π^-)

Table 1: L/T Separation Kinematics

Kinem.	Q^2 $\frac{\text{GeV}^2}{c^2}$	W GeV	E GeV	E' GeV	θ_e deg	θ_k deg	P_K $\frac{\text{GeV}}{c}$	ϵ	t GeV ²
2a	2.0	1.8	3.245	0.922	48.27	14.65	1.625	0.402	-0.81
2b	2.0	1.8	4.045	1.722	31.08	19.08	1.625	0.636	-0.81
2c	2.0	1.8	6.045	3.722	17.15	23.79	1.625	0.856	-0.81
2d	2.0	2.0	3.645	0.917	45.51	12.50	2.186	0.376	-0.55
2e	2.0	2.0	4.845	2.117	25.51	17.26	2.186	0.674	-0.55
2f	2.0	2.0	6.045	3.317	18.17	19.67	2.186	0.805	-0.55
2g	2.0	2.2	4.045	0.869	44.31	12.50	2.724	0.333	-0.42
2h	2.0	2.2	4.845	1.669	28.79	13.37	2.724	0.557	-0.40
2i	2.0	2.2	6.045	2.869	19.55	16.03	2.724	0.736	-0.40
2.5a	2.5	1.8	3.645	1.055	47.54	14.87	1.790	0.412	-1.01
2.5b	2.5	1.8	4.845	2.255	27.67	20.20	1.790	0.691	-1.01
2.5c	2.5	1.8	6.045	3.455	19.92	22.83	1.790	0.815	-1.01
2.5d	2.5	2.0	4.045	1.050	45.11	12.69	2.379	0.387	-0.70
2.5e	2.5	2.0	4.845	1.850	30.62	16.16	2.379	0.592	-0.70
2.5f	2.5	2.0	6.045	3.050	21.22	19.03	2.379	0.756	-0.70
2.5g	2.5	2.2	4.845	1.403	35.31	12.50	2.934	0.462	-0.51
2.5h	2.5	2.2	6.045	2.603	22.99	15.57	2.934	0.678	-0.51
3a	3.0	1.8	4.045	1.189	46.52	14.97	1.952	0.421	-1.22
3b	3.0	1.8	4.845	1.989	32.40	18.60	1.952	0.614	-1.22
3c	3.0	1.8	6.045	3.189	22.75	21.67	1.952	0.767	-1.22
3d	3.0	2.0	4.400	0.756	58.20	12.50	2.569	0.385	-0.85
3e	3.0	2.0	4.845	1.584	36.43	14.76	2.569	0.504	-0.85
3f	3.0	2.0	6.045	2.784	24.37	18.13	2.569	0.702	-0.85
3g	3.0	2.2	5.200	1.491	36.24	12.50	3.143	0.455	-0.62
3h	3.0	2.2	6.045	2.336	26.65	14.83	3.143	0.615	-0.62

rates computed for the same kinematics (this is an overestimate by up to a factor of 2 of the (e, π^+) rates, making it a conservative estimate). Times were calculated for 10^4 counts for all kinematics (except for the backward angle at $Q^2=2.0$ and 3.0 , some of which were calculated for 2.5×10^3 counts as marked).

The coincidence cross sections and rates were determined using the model of ref.[3] for Λ production which fit the Hall C data taken last year. For L/T separation kinematics, where t is a minimum, model wjc4 gives cross sections lower by 2–3 but, as already discussed, is less accurate in reproducing the (few) existing data at high Q^2 . [In the case of the t -dependence kinematics, as considered before, the disagreement between the models relies on the opposite slope they are predicted to have.] Additionally the Σ^0 will fall within our missing mass acceptances. The statistics will be somewhat worse due to smaller cross sections. Yields for a subset of the kinematics were checked with the Monte Carlo code MCEEP which explicitly performs the averaging over the acceptances of both the hadron and electron arms; the two approaches gave roughly comparable rates.

Tables 5 and 6 show the rates and times for the σ_{LT} and t -dependence measurements (respec-

Table 2: σ_{LT} Separation Kinematics

Kinem.	$\frac{Q^2}{c^2}$	W GeV	E GeV	E' GeV	θ_e deg	θ_k deg	P_K $\frac{GeV}{c}$	t GeV ²	Θ_{cm} deg
2g	2.0	2.0	6.045	3.317	18.17	26.86	2.47	-0.87	38.76
2h	2.0	2.0	6.045	3.317	18.17	12.50	2.47	-0.87	38.76
2.5g	2.5	2.2	6.045	2.603	22.99	18.64	2.91	-0.57	12.41
2.5h	2.5	2.2	6.045	2.603	22.99	12.50	2.91	-0.57	12.41
3g	3.0	2.0	6.045	2.784	24.67	23.58	2.44	-1.08	28.31
3h	3.0	2.0	6.045	2.784	24.67	12.50	2.44	-1.08	28.31

Table 3: t -dependence Kinematics

Kinem.	$\frac{Q^2}{c^2}$	W GeV	E GeV	E' GeV	θ_e deg	θ_k deg	P_K $\frac{GeV}{c}$	t GeV ²	Θ_{cm} deg
2j	2.0	2.2	6.045	2.87	19.55	24.29	2.56	-0.70	30
2k	2.0	2.2	6.045	2.87	19.55	32.26	2.18	-1.40	58
2l	2.0	2.2	6.045	2.87	19.55	38.14	1.85	-2.00	75
2m	2.0	2.2	6.045	2.87	19.55	42.17	1.63	-2.40	86
3i	3.0	2.2	6.045	2.34	26.65	18.05	3.10	-1.40	18
3j	3.0	2.2	6.045	2.34	26.64	30.34	2.40	-2.00	63
3k	3.0	2.2	6.045	2.34	26.64	33.22	2.18	-2.40	73
3l	3.0	2.2	6.045	2.34	26.64	37.66	1.85	-3.00	87

tively). Count rates and cross sections were computed the same way as in Table 4. Shown is the total time for each setting, taking into account the kaon survival fraction for each momentum setting of the kaon spectrometer, for both the singles rates and the coincidence rates. [The kaon momentum ranges from 1.4 GeV/c to 3.1 GeV/c, corresponding to 10–36% survival fractions for the HRS flight path.] Count rates assume an incident beam current of 75 μ A, on a 15 cm LH2 target, and a 6.0 msr solid angle for each HRS2 spectrometer.

Pions in the electron arm will be rejected by a combination of lead-glass and gas Cerenkov; a combined rejection factor of 200:1 was assumed in calculations (the system has been shown capable of performing with rejections of 500:1). A loose cut will be used to reduce electron-arm trigger rates as well. Pions in the hadron arm will be rejected by the aerogel (and coincident pions partially by time-of-flight also). Cerenkov rejection ratios of 50:1 were assumed (100:1 is the goal of the system). To reject protons time-of-flight alone will be sufficient (both single arm and for coincident protons double arm timing will be used). The signal-to-noise ratio was computed by computing the kaon single arm (e,K) rates using the procedure suggested in [43], and using a 2 ns resolving time. The kaon single arm rates were averaged over the spectrometer angular acceptances and the survival fraction of the kaons was taken into account at each spectrometer setting. No cuts on missing mass were assumed in calculating the signal-to-noise.

Table 4: L/T Rates and counting times

Kinem.	(e,e'K) nb/GeV/sr ²	(e,e'K) s ⁻¹	(e,e') s ⁻¹	(e, π^-) s ⁻¹	(e,p) s ⁻¹	(e, π^+) s ⁻¹	(e,K) s ⁻¹	S/N	time hours
2a	0.19	0.02	0.57×10^3	23.5×10^4	1.25×10^5	2.77×10^5	6900	3	35*
2b	0.55	0.11	2.73×10^3	16.8×10^4	1.17×10^5	1.87×10^5	4600	4	25
2c	2.32	1.00	23.1×10^3	13.1×10^4	1.22×10^5	1.43×10^5	3500	6	3
2d	0.22	0.04	0.59×10^3	13.1×10^4	0.69×10^5	1.53×10^5	3800	9	17*
2e	1.02	0.42	4.77×10^3	8.52×10^4	0.61×10^5	0.94×10^5	2300	19	7
2f	2.39	1.56	16.1×10^3	7.27×10^4	0.61×10^5	0.78×10^5	1900	25	2
2g	0.20	0.05	0.54×10^3	4.74×10^4	0.31×10^5	0.56×10^5	1200	38	15*
2h	0.52	0.23	2.60×10^3	7.23×10^4	0.42×10^5	0.80×10^5	2000	22	12
2i	1.41	1.07	10.6×10^3	5.70×10^4	0.39×10^5	0.61×10^5	1500	31	3
2.5a	0.36	0.05	0.40×10^3	20.0×10^4	1.10×10^5	2.30×10^5	5700	11	52
2.5b	1.67	0.53	2.69×10^3	11.9×10^4	0.95×10^5	1.32×10^5	3300	30	6
2.5c	3.94	1.91	8.66×10^3	10.0×10^4	0.94×10^5	1.09×10^5	2700	41	2
2.5d	0.40	0.09	2.22×10^3	11.1×10^4	0.59×10^5	1.27×10^5	3100	7	29
2.5e	1.24	0.51	1.73×10^3	7.10×10^4	0.49×10^5	0.78×10^5	1900	77	6
2.5f	3.35	2.27	6.49×10^3	5.26×10^4	0.44×10^5	0.57×10^5	1400	125	2
2.5g	0.21	0.08	0.92×10^3	5.96×10^4	0.34×10^5	0.66×10^5	1600	27	33
2.5h	0.65	0.49	4.37×10^3	4.09×10^4	0.28×10^5	0.44×10^5	1100	51	6
3a	0.10	0.01	0.29×10^3	17.1×10^4	0.97×10^5	1.94×10^5	4800	4	15*
3b	0.69	0.23	1.05×10^3	11.1×10^4	0.83×10^5	1.23×10^5	3100	35	13
3c	1.80	0.94	3.66×10^3	8.26×10^4	0.76×10^5	0.89×10^5	2200	58	3
3d	5.84	0.48	0.30×10^3	9.31×10^4	0.50×10^5	1.05×10^5	700	1000	8
3e	11.9	4.66	0.67×10^3	6.74×10^4	0.43×10^5	0.75×10^5	1900	1800	2
3f	38.9	26	2.90×10^3	4.23×10^4	0.35×10^5	0.46×10^5	1100	4000	2
3g	0.07	0.03	0.63×10^3	4.79×10^4	0.27×10^5	0.53×10^5	1300	18	22*
3h	0.14	0.10	1.94×10^3	3.30×10^4	0.22×10^5	0.35×10^5	900	28	27

Times are for 10^4 counts except * which are 2.5×10^3 counts.

Table 5: σ_{LT} rates and counting times

Kinem.	(e,e'K) nb/GeV/sr ²	(e,e'K) s ⁻¹	(e,e') s ⁻¹	(e, π^-) s ⁻¹	(e, π^+) s ⁻¹	(e, π^+) s ⁻¹	(e,K) s ⁻¹	S/N	time hours
2g	5.62	3.77	16.2×10^3	7.27×10^4	0.59×10^4	0.36×10^4	90	1300	2
2h	4.51	2.50	16.2×10^3	7.27×10^4	11.4×10^4	28.9×10^4	7200	11	2
2.5g	0.866	0.97	4.37×10^3	4.09×10^4	1.38×10^4	1.53×10^4	380	290	4
2.5h	0.510	0.82	4.37×10^3	4.09×10^4	5.85×10^4	13.2×10^4	1180	79	4
3g	0.49	0.59	2.90×10^3	4.23×10^4	1.47×10^4	11.9×10^4	2900	35	2
3h	0.42	0.51	2.90×10^3	4.23×10^4	11.9×10^4	30.4×10^4	7600	12	2

Table 6: t -dependence rates and counting times

Kinem.	(e,e'K) nb/GeV/sr ²	(e,e'K) s^{-1}	(e,e') s^{-1}	(e, π^-) s^{-1}	(e,p) s^{-1}	(e, π^+) s^{-1}	(e,K) s^{-1}	S/N	time hours
2j	9.12	2.90	10.6×10^3	5.70×10^4	8.52×10^3	6.21×10^3	155	880	2
2k	9.90	5.56	10.6×10^3	5.70×10^4	4.73×10^3	2.19×10^3	55	4700	2
2l	13.2	5.66	10.6×10^3	5.70×10^4	5.41×10^3	2.25×10^3	56	4700	2
2m	14.2	4.76	10.6×10^3	5.70×10^4	7.05×10^3	3.07×10^3	77	2900	2
3i	0.30	0.34	1.94×10^3	3.30×10^4	10.1×10^3	11.2×10^3	280	300	13
3j	1.64	0.86	1.94×10^3	3.30×10^4	3.01×10^3	1.42×10^3	36	8000	4
3k	1.86	0.85	1.94×10^3	3.30×10^4	3.65×10^3	1.59×10^3	40	8000	4
3l	1.99	0.69	1.94×10^3	3.30×10^4	6.07×10^3	2.57×10^3	64	2700	4

4 Detector Performance and Error Analysis

4.1 Monte Carlo simulation and Particle IDentification (PID)

A Monte Carlo code has been developed to simulate the “results” of the proposed experiment. Besides the reconstruction of the usual phase space variables, the simulation is based on the reconstruction of the coincidence time spectra and the Missing Mass spectra as they will be reconstructed in the actual analysis, when the data come from different sources.

Here we have taken into account seven “event types”:

- 1) $(e, e'\pi^+)$ RANDOM COINCIDENCES from singles $(e, e') \otimes (e, \pi^+)$
- 2) $(e, e'K^+)$ RANDOM COINCIDENCES from singles $(e, e') \otimes (e, K^+)$
- 3) $(e, e'p)$ RANDOM COINCIDENCES from singles $(e, e') \otimes (e, p)$
- 4) $(e, e'\pi^+)$ TRUE COINCIDENCES in the continuum of the Missing Mass spectra
- 5) $(e, e'K^+)$ TRUE COINCIDENCES in the continuum of the Missing Mass spectra
- 6) $(e, e'p)$ TRUE COINCIDENCES in the continuum of the Missing Mass spectra
- 7) $(e, e'K^+)$ **TRUE COINCIDENCES with a bound state residuum**

Different sources of background are therefore taken into account, and the code is versatile enough to allow for different selection criteria on the particles, like, for example, PID. As an example, a pion can be TOTALLY rejected or rejected only with a given factor (i.e. 5% is a reasonable number with a threshold aerogel Cerenkov counter) or not rejected at all.

Events with particles other than electrons in the electron arm are not considered. This is due to the excellent rejection for π^- (and heavier hadrons) that can be reached making use of the CO_2 gas Cerenkov detector and the shower counter. Operated in the threshold mode, the Cerenkov counter has been demonstrated [49] to give pion rejection ratios upto 10^3 . The dominant background (knock-on electrons) will be reduced another 2 orders of magnitude by the lead-glass shower counters, giving a total pion rejection ratio of $\geq 10^5$ – higher than required for this experiment.

INPUT for the Monte Carlo are :

- Acquisition Time
- The kinematical settings
- (e, e') , (e, π^+) , (e, K^+) , (e, p) single rates (in sec^{-1})
- $(e, e'\pi^+)$, $(e, e'K^+)$, $(e, e'p)$ coincidence rates in the continuum (in sec^{-1})
- $(e, e'K^+)$ TRUE coincidence rates in **bound states** (in sec^{-1}) and the Missing Mass positions
- Acceptances of the spectrometers

- Resolutions (Beam, momenta, angles, coincidence–time)

A reduction of the random coincidences rates (coincidence events coming from singles such as $(e, e') \otimes (e, h)$ with h being any hadron) has been considered for the extended target case by requesting that the two arms both point to the same vertex position along the target. In this case the vertex reconstruction resolution comes into the game. A resolution of 3 mm in the direction perpendicular to the spectrometers has been used. This resolution is then projected along the target (thus depending on the kinematical settings) and on an event-by-event basis the position along the target Z_{targ} is extracted for both arms. The variable $\Delta_{vertex} = Z_{targ_ele} - Z_{targ_hadr}$ is then computed and the events are accepted only in the range $\pm 4\sigma(\Delta_{vertex})$. In such a way the random coincidences rates are reduced by a factor $8\sigma(\Delta_{vertex})/Target_{length}$.

In the following, the results obtained for the kinematics “2.5e” of Table 1 are reported. This kinematics can be considered as a typical case of our experiment. All the shown spectra already contain a reduction of the random coincidence events for an extended target as just explained. Numerically, such a reduction is, for this kinematics, a factor $8\sigma/Target_{length} = 8 \times (5.2mm)/(150mm) = 0.28$.

First, the results obtained without any PID selection will be shown. Then the improvements achieved with a PID selection with efficiencies (able to reduce to 5% both pion and proton rates) will be shown. Then, results from our “worst” case (as far as the signal to noise ratio) will also be shown (kinematic 2a of table 1). At last it will be discussed (next section) how a kaon/pion and kaon/proton rejection at the level of 5% can be obtained.

The main assumption under which the simulation has been performed are:

- TOTAL COINCIDENCE TIME = 50 ns
- Resolution of the COINCIDENCE TIME = 1 ns FWHM
- Path Length from target to timing defining detector assumed = 25 m
- Target length = 15.0 cm
- Rates for REAL COINCIDENCES $(e, e'\pi^+)$, $(e, e'K^+)$ and $(e, e'p)$ in the **continuum** (of the Missing Mass spectrum) are just estimates, since we didn't compute the cross sections for all the participating processes. Moreover, in these cases the events are allowed to fill the Missing Mass spectra as if they were random coincidences. Such an assumption, i.e., a “smooth” missing mass distribution, could for example come from quasi-elastic production and is true in the data taken in Hall A in November 97, where $(e, e'\pi^+)$ events spread over the missing mass spectrum according to the phase space acceptance. Of course, this assumption depends on the kinematical choice.

Anyway, the main sources of background are the random coincidences $(e, e') \otimes (e, \pi^+)$ and $(e, e') \otimes (e, p)$, which are, of course, distributed randomly according to the phase space probability, and, as will be seen can be easily subtracted.

In figures 15 and 16 the results from 1 hour of data taken at the luminosity of the experiment for kinematics 2.5e of table 1, are reported. NO PID selection has been performed and the coincidence timing spectrum (fig. 15(a)) shows the $(e, e'K^+)$ peak “hidden” in both the background of random

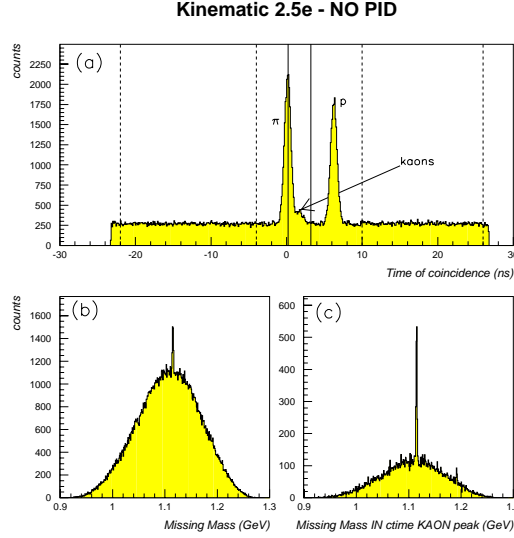


Figure 15: Monte Carlo simulation for kinematic 2.5e table 1. Random coincidence events reduction for extended target already included. (a) Timing spectrum: solid lines select a cut for events “IN the kaon peak”, dashed lines select events “OFF kaon peak” used for subtraction. (b) Missing Mass spectrum for all the events entering spectrum (a). (c) Missing Mass spectrum for events “IN the kaon peak”.

coincidences (flat in coincidence time) and real ($e, e'\pi^+$) events. However the figure also shows that when a cut in the kaon coincidence peak is considered, background events are spread all over the missing mass spectrum according to the phase space acceptance, and the peaks of the exclusive $p(e, e'K^+)\Lambda$ and $p(e, e'K^+)\Sigma$ transitions show up. From fig. 16(a) in the Λ peak, a signal to noise ratio $S/N > 4$ is obtained and the background subtraction can be easily performed (16(c)). It has to be noted that the missing mass spectrum actually acts like an effective PID tool.

Clean particle identification of the kaon is anyway a big help for this experiment and the effect of a PID selection giving a contamination of 5% pions and protons is shown in figs. 17 and 18. The figures have been obtained in exactly the same way of figs. 15 and 16, but for the cut on pions and protons. From fig. 18(a) in the Λ peak, $S/N > 20$ is now obtained.

Finally the results obtained in the case of kinematic 2a of table 1 representing the kinematic with the lowest S/N ratio of the proposed experiment are reported in figs. 19 and 20. The spectra simulate 10 hours data acquisition (our request is for 35 hours). The effect of PID is shown. Reducing the errors of the background subtraction as shown passing from fig. 20(a) to fig. 20(b) is especially crucial to identify the Σ production peak, which turns to be suppressed by the hadron arm acceptance. In fact, since the Σ peak isn't placed at the “center” of the phase space acceptance, meaning electron arm and hadron arm kinematics do not match and counting rates for the Σ are (for this kinematic) suppressed by almost one order of magnitude with respect to the cross section estimate.

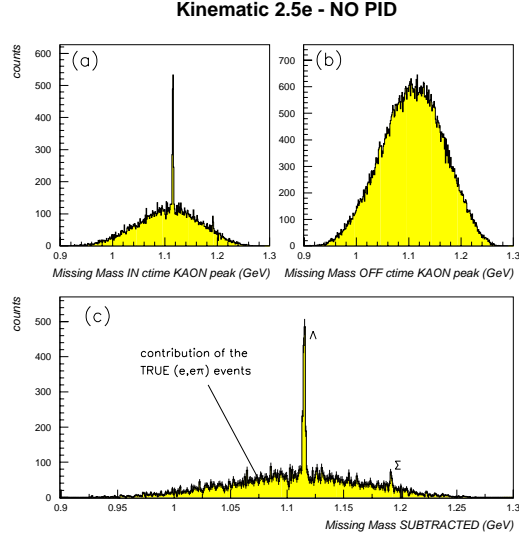


Figure 16: Missing Mass: (a) selected events “IN coincidence time kaon peak”; (b) selected events “OFF coincidence time kaon peak”; (c) Subtracted spectrum.

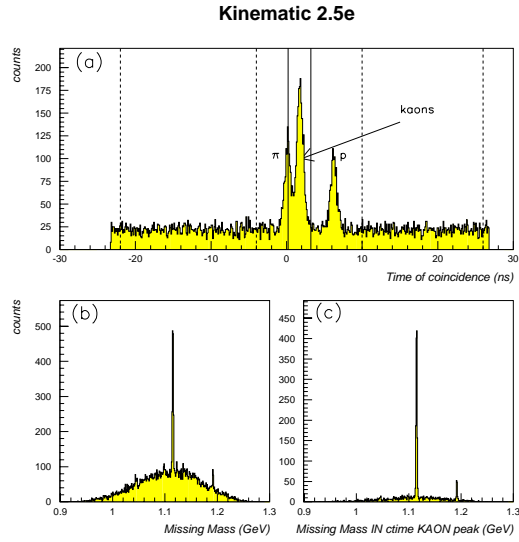


Figure 17: Same as fig. 15 but with a reduction of π and protons by a factor 0.05 (from PID)

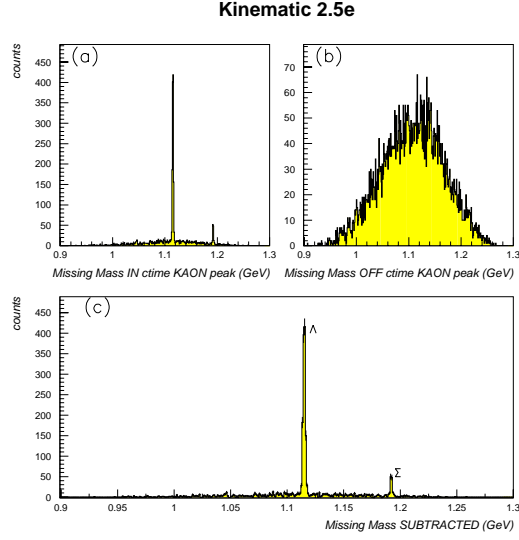


Figure 18: Same as fig. 16 but with a reduction of π and protons by a factor 0.05 (from PID)

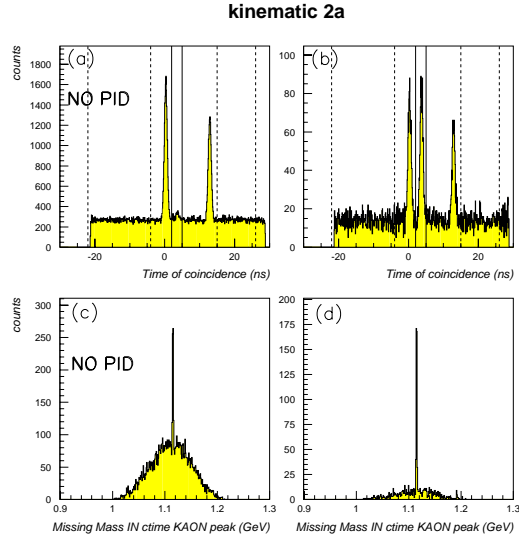


Figure 19: Monte Carlo simulation for kinematic 2a table 1. Random coincidence events reduction for extended target already included. In case of spectra (a) and (c) no PID selection has been applied, while a reduction of π and protons by a factor 0.05 (from PID) has been applied for spectra (b) and (d).

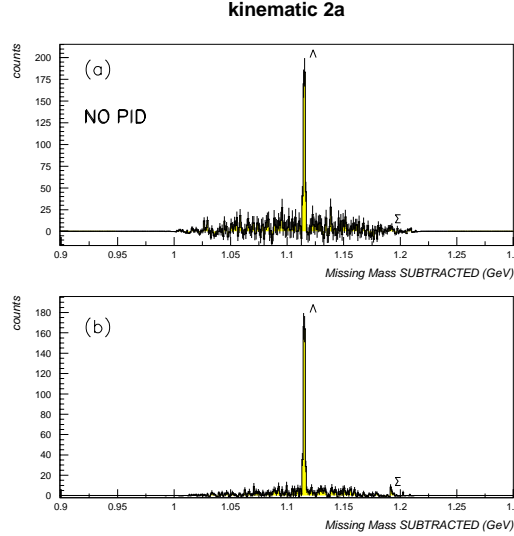


Figure 20: Missing Mass subtracted spectra for kinematic 2a table 1 without any PID selection (a) and with PID selection (b).

4.2 Particle Identification - Aerogel threshold Cerenkov Counters

The standard equipment of Cerenkov aerogel counters are used in the focal plane package detector to discriminate pions from protons. Silica aerogel, with index of refraction $n = 1.025$, enables this separation from 0.62 to 4 GeV/c. A prototype and the final detector have been tested [50, 51, 52]. The detector is of the reflective type and consists of 13 sections made of two planar parabolic mirrors, viewed by 26 5" BURLE 8854 photomultipliers [50].

The efficiency measured in tests with 100 MeV electron beam was better than 99% (number of photoelectron = $n_{pe} = 6.9$). These results have been confirmed in tests performed at CERN PS with beam of positrons, pions and protons [52]. The p.e. number as well as the efficiency, evaluated at an optimal threshold setting, were lower for pions ($\sim 96\%$), with an estimated p/π rejection ratio of $\sim 5\%$. Improvements with respect to these results have been already obtained baking the aerogel (i.e. removing the moisture and consequently improving the optical quality). Beam tests performed with baked material show a significant increase in the total number of p.e. detected for pions. The analysis is still in progress [52].

Even better results have subsequently been obtained using a diffusion box detector. A prototype box has been built, its dimension being $45 \times 45 \times 25 \text{ cm}^3$, and equipped with six 5" Burle 8854 PM arranged in two rows of three phototubes opposite to each other, collecting the Cerenkov light produced by a layer of aerogel, which is similar in the design to the Cerenkov detector now operating successfully in Hall C.

The diffusion material used was millipore paper. A preliminary analysis of tests performed at CERN demonstrates that using a 6 cm thick aerogel layer with $n = 1.025$ we can get an integrated number of 7.5, and 11.0 p.e. for 5 GeV/c π and e , respectively. Aerogel of better quality is now available and preliminary measurements with $n = 1.015$ have also been done with the diffusion box prototype with cosmic rays. A $n_{pe} = 7.0$ has been measured [53] with only 6 cm of aerogel,

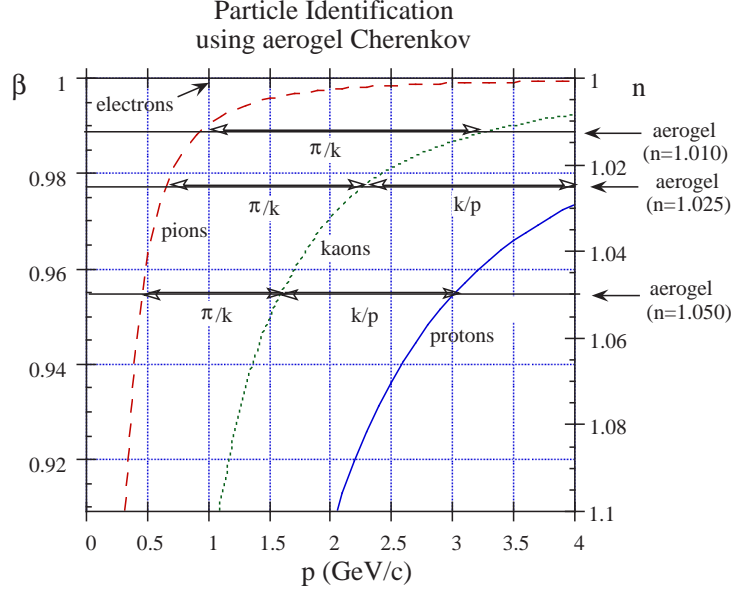


Figure 21: PID with threshold aerogel Cherenkov counters

quite good for such low refractive index material. Of course increasing the thickness of the radiator improves the performances. Further work is underway for a possible optimization of this detector and an agreement to build such a detector in a joint effort between CEBAF and INFN has been made.

Particle identification for kaons in the momentum range $1.6 - 3.0$ GeV/c can be performed using two threshold Cherenkov counters with different indices of refraction. In fig. 21 the velocity β vs the momentum of pions, kaons and protons is reported. In the axis on the right $n = 1/\beta$ is shown which represent the index of refraction at threshold for a given momentum. The figure shows that with the choice of $n = 1.05$ it is possible to separate kaons (above threshold) from protons (below threshold) in the range $1.6 - 3.0$ GeV/c. Using $n = 1.01$ allows the separation between pions and kaons so that the combination of the two allows to identify the kaons.

The tests we have performed with suitable extrapolation from the electron, pion and proton case to the kaon case, show that the use of two aerogel Cherenkov counters with index of refraction $n = 1.05$ and $n = 1.01$, either of the reflective type (which is already existing) or even better, of the diffusion box type (now under construction), will allow us to reach the required performances. On the other hand a rejection factor at the level of 5% for particles below threshold is consistent with what can be found in literature for this type of detectors (e.g. see ref. [55]).

The idea is to use the existing reflective type counter already installed in the hadron arm, to move out the Gas Cherenkov of the hadron arm (useless in this experiment), and to replace it with the other aerogel counter which could be either the “standard” one being part of the electron arm detector package, or the new diffusion box. The two detectors will be filled with aerogel of index of refraction $n = 1.01$ and $n = 1.05$ of the better quality now available on the market. In fact, the recent development of a new production technique for aerogels [54], has improved the optical quality of this material with respect to samples produced with the standard method.

Table 7: L/T Separation Statistical Uncertainty

Kinem.	Q^2 (GeV/c) ²	σ_T nb/sr	$\Delta\sigma_T$ %	σ_L nb/sr	$\Delta\sigma_L$ %
2a-c	2.0	79.6	4.7	53.0	7.0
2d-f	2.0	89.1	4.6	43.6	7.0
2g-i	2.0	89.8	4.5	25.6	7.0
2.5a-c	2.5	63.2	3.0	44.2	5.0
2.5d-f	2.5	70.6	3.1	35.5	5.4
2.5g-h	2.5	67.1	5.3	14.9	9.3
3a-c	3.0	51.9	5.6	36.9	8.7
3d-f	3.0	57.9	3.4	29.2	6.3
3g-h	3.0	46.0	10	4.8	19

Table 8: $\langle \cos \phi \rangle$ Asymmetry Statistical Uncertainty

Kinem.	Q^2 (GeV/c) ²	A	ΔA %	$\Delta\sigma_{LT}$ %
2g-h	2.0	0.076	3.6	6.0
2.5g-h	2.5	0.079	3.5	5.8
3g-h	3.0	0.077	3.6	5.5

It has to be anyway emphasized that even a higher rejection ratios (i.e. 10%) for pions and protons, allows one to carry out the experiment successfully as has been demonstrated from the simulations reported in the previous section.

4.3 Statistical Uncertainties

The fraction of the (e,e' K⁺) final states which have only a single Λ in them ranges between 50–60% over our kinematics; the fraction of (e,e' K⁺) final states which have only a single Σ^0 in them are approximately 15% of the total number. The remainder are continuum states with more than 1 particle or higher resonances. The statistics will allow the measurement of (for the $(e+p \rightarrow e'+K^++\Lambda)$ channel) the full cross section with a 1–2% statistical uncertainty; the statistical uncertainty on the extracted values of σ_L and σ_T is given in Table 7. [The $(e+p \rightarrow e'+K^++\Sigma^0)$ channel will have statistical uncertainties approximately 3 times as large.] Tables 8 and 9 show the uncertainties for the $\langle \cos \phi \rangle$ and Λ dependence kinematics, respectively.

4.4 Systematic Uncertainties

The systematic uncertainties contribute differently to the three types of measurements. The systematical uncertainties which are most important however are the relative errors, not the absolute uncertainties since the physics will be extracted by comparing measured cross sections. The absolute normalization of the data set requires the absolute uncertainty.

Table 9: t -dependence Statistical Uncertainty

Kinem.	Q^2 (GeV/c) ²	t GeV ²	$d\sigma_v/d\Omega_k$ nb/GeV/sr ²	$\Delta d\sigma_v/d\Omega_k$ %
2j	2.0	-0.70	1.03	1.0
2k	2.0	-1.40	0.65	1.0
2l	2.5	-2.00	0.66	1.0
2m	2.5	-2.40	0.40	1.0
3i	3.0	-1.40	0.43	1.0
3j	3.0	-2.00	0.29	1.0
3k	3.0	-2.40	0.17	1.0
3l	3.0	-3.00	0.17	1.0

Table 10: Systematic Point-to-Point Uncertainties

Scattering Angles	0.3%
Target Density Variations	0.2%
Cell Walls	0.2%
K^+ absorption	1.0%
Detector Inefficiencies	2.0%
Kaon Decay	0.5%
Radiative Corrections	1.0%
Beam Current	0.5%
Acceptances	1.0%
Total	2.8 %

Table 11: Systematic Scale Uncertainties

Kinematics (angles,energies)	2.0%
Target Density Variations	0.5%
Cell Walls	0.5%
K^+ absorption	2.0%
Detector Inefficiencies	2.0%
Kaon Decay	1.0%
Radiative Corrections	1.0%
Beam Current	1.0%
Acceptances	2.0%
Total	4.4 %

The errors which contribute to the general normalization are referred to as scale errors and will raise or lower both longitudinal and transverse cross sections together. Examples are the overall target density, the beam current calibration, spectrometer absolute acceptances, K^+ absorption, detector inefficiencies, etc.

The errors which contribute to the separation of the responses are referred to as the point-to-point errors and include any differences between K^+ absorption at the forward and backward angles (although the spectrometer is at the same central momentum, the phase space is larger at the higher energy and populated differently), knowledge of the relative acceptance, relative luminosity, relative detector inefficiencies, etc.

To set the scale, the recent Hall C experiments[23, 22] had 2-3% point-to-point uncertainties and an overall scale uncertainty of 5%. Shown in Table 10 are the contributions to the extracted response functions of the RELATIVE point-to-point uncertainties between successive measurements. We expect to do similar to the accomplished Hall C experiment, as we do also in the absolute scale uncertainties shown in Table 11.

We have also investigated the effects of the Hall A resolutions using the numbers obtained last summer during the $^{16}\text{O}(\text{e},\text{e}'\text{p})$ experiment of focal plane positions of 200 microns, focal plane angular resolutions of 0.4 mrad which translate to target resolutions of 2.0 mrad horizontal and 6.0 mrad vertical, position resolution of 3.0 mrad and momentum resolution of 2×10^{-4} . Plotted in Figure 22 is the forward and backward angle plots of the invariant mass W versus the four-momentum transfer squared Q^2 . What is seen is that the overlap of kinematics is far from perfect, with the lower energy angle having less phase space. This is taken into account in our count rate estimates. The angular resolution affects our ability to bin in Q^2 , and therefore the missing mass resolution. However since this is a hydrogen experiment, missing mass resolution of 2-5 MeV is fine.

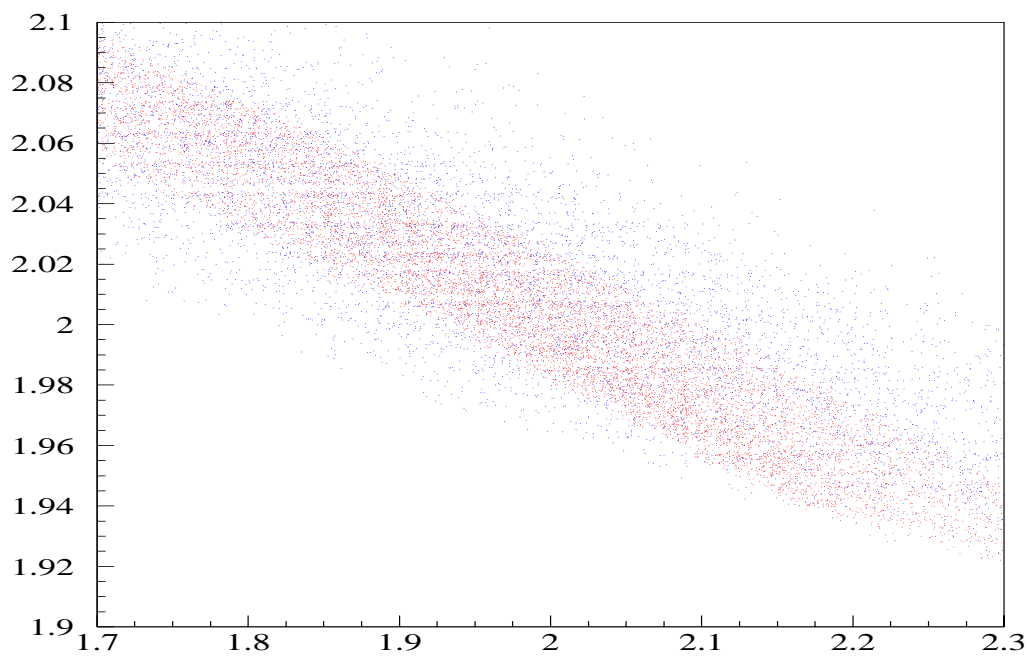


Figure 22: The four-momentum transfer squared (in $(\text{GeV}/c)^2$ on the x-axis) versus the invariant mass W (in GeV on the y-axis) for backward (the narrow central band) and forward (the wide band) angles.

5 Runplan and Beamtime Summary

Table 12: Beam Time Summary

Set-up/Check-out	50 hours
DAQ for L/T separations	349 hours
DAQ for σ_{LT}	16 hours
DAQ for t -dependence	33 hours
Field Changes	38 hours
Empty Target	10 hours
Energy Changes	20 hours
Total	520 hours

The beam time summary is reported in Table 11. The additional time needed for overhead is fairly small: spectrometer field changes are estimated to total 38 hours, 50 hours of set-up and check out is required, and short empty target run at each setting gives another 10 hours. Added with the 406 DAQ hours and 20 hours (5 energies at 4 hours per energy change) of time for accelerator energy changes, the total beam time request of 520 hours as shown in Table 4. To minimize overhead, it is assumed that all points at a given incident energy will be measured, moving the spectrometer accordingly, before changing energies. In particular, the σ_{LT} response function and the t -dependence will be measured before changing the electron angle or momentum to minimize the systematic uncertainties.

As can be seen from Tables 4-6, the signal-to-noise is excellent at all kinematics. The rates in the focal plane of the spectrometers are low, meaning we could run with higher luminosity if it was available. [The tapping rates vary from 100 Hz to 800 Hz. At the higher tapping rates the kaon cross section is also high and we can lower the current if desired for deadtime reasons.] The cuts on the missing mass spectrum will be done in replay, not the trigger, enabling one to obtain data on additional exclusive channels. [No estimates were given for the statistical uncertainties associated with these additional channels because of the small yields involved.] The signal-to-noise for a particular final state will be larger than for the entire spectrum.

Pion data will be taken in prescale mode. This is important not only to tell us the shape of the backgrounds, but also because many of the physics arguments given are general to pseudo-scalar meson production. The use of the pion final states will provide additional constraints on the theory. The pion coincidence rates are considerably higher than the kaon rates; the statistical uncertainty will be less important.

References

- [1] M. Bockhurst *et al.*, Z. Phys. C 63 37 (1994).
- [2] Private Communication and G. Niculescu *et al.*, submitted to Phys Rev. C, (1998).
- [3] J.C. David, C. Fayard, G.H. Lamot, B. Saghai, Phys. Rev. C 53 2613 (1996).
- [4] R. A. Adelseck, B. Saghai, Phys. Rev. C 42 108 (1990).
- [5] P. Feller, *et. al.*, Nucl. Phys. B39 413 (1979).
- [6] M. Bockhurst *et al.*, Contributed Paper, Few Body XIV, 551 (1994).
- [7] P. Brauel *et al.*, Z. Physik, 3, 101 (1979).
- [8] A. Bodek *et al.*, Phys. Lett. 51B, 417 (1974).
- [9] J. Ashman *et al.*, Nucl. Phys. B328, 1 (1989).
- [10] R. A. Williams, C-R Ji and S. R. Cotanch, Phys. Rev. C 46 1617 (1992).
- [11] C.B. Dover, G.E. Walker, Phys. Rep. 89 1 (1982).
- [12] J. Adam, J. Mares, O. Richter, M. Sotona, S. Frullani, Czech. J. Phys. 42 1167 (1992).
- [13] L. S. Celenza, A. Pantirix, C. M. Shakin, and Hui-Wen Wang, Phys. Rev. C 41 366 (1990).
- [14] G.R. Farrar, K.Huleihel, H.Zhang, Nucl. Phys. B349, 655 (1991).
- [15] M. Schuermann, Thesis, Wuppertal University (1992).
- [16] T. Azemoon *et al.*, Advance in Nucl. Phys. 17, 47 (1987).
- [17] S. Frullani, *et. al.*, MPS, INFN-ISS 90/5, (1990).
- [18] R. G. Arnold *et al.*, Phys. Rev. Lett., 52, 727 (1984).
- [19] P.E. Ulmer, MCEEP, priv. comm., <http://www.physics.odu.edu/ulmer/mceep/mceep.html>.
- [20] E89004, R. Schumacher Spokesperson, Hyperon Photoproduction, Hall B.
- [21] E93050, M.Mestaeyer, Measurement of Structure Functions for Kaon Electroproduction.
- [22] E91016, B. Zeidman, Electroproduction of Kaons and Light Hypernuclei.
- [23] E93018, O.K. Baker, Longitudinal/Transverse Separation in Kaon Electroproduction.
- [24] M.Iodice *et. al.*, Proceedings of “Diquark-96”, Torino (Italy), Oct. 28-30, 1996
- [25] P.Kroll, M.Schurmann, K.Passek, W.Schweiger, Phys. Rev. D 55 4315 (1997).
- [26] S. R. Cotanch and S. S. Hsiao, Nucl. Phys. A 450 4192 (1986).
- [27] C-R Ji and S. R. Cotanch, Phys. Rev. D 41 2319 (1990).

- [28] R.A.Williams, C.R.Ji, S.R.Cotanch., Phys. Rev. D 41 1449 (1990).
- [29] C. J. Bebek *et al.*, Phys. Rev. D 15, 47 (1977).
- [30] T. Sjöstrand, Comp. Phys. Commun. 39, 347 (1986).
- [31] F.S. Dietrich, C.W. Johnson, 1986 CEBAF Summer Study, RPAC II, 389 (1986).
- [32] B. Andersson *et al.*, Phys. Rep. 97, 31 (1983).
- [33] R.L.Anderson *et al.*, Phys.Rev. D 14 679 (1976).
- [34] O.K. Baker, Hampton Univeristy HUPHY-03-92 (1992).
- [35] R.C.E. Devenish, D.H. Lyth, Phys. Rev. D 5 47 (1972).
- [36] E.B. Dally *et. al.*, Phys. Rev. Lett. 45 232 (1980).
- [37] F. Cardarelli *et. al.*, Phys. Lett. B 332 1 (1994).
- [38] R. N. Cahn, Phys. Lett. 78B, 269 (1978).
- [39] E. L. Berger, Z. Phys. C4, 289 (1980).
- [40] A. Brandenburg, V.V. Khoze, D. Müller, Phys. Lett. B 347 413 (1995).
- [41] C. C. Chang, computer code XSECDEEP, private communication (1993).
- [42] C. C. Chang and P. Markowitz, computer code PIXSEC, private communication (1993).
- [43] C.E. Hyde-Wright, W. Bertozzi, J.M. Finn, 1985 CEBAF Workshop, NN, Virginia (1985).
- [44] R. E. Taylor, Electron and Photon Interactions, Liverpool, Daresburg, 251 (1969).
- [45] C. C. Chang AIP 269 51 460 (1992).
- [46] S. J. Brodsky, Plenary Talk, Workshop on CEBAF at Higher Energies, (1994).
- [47] F. Schlumpf, SLAC-PUB-6483 (1994).
- [48] A. Calogeracos, N. Dombey, G. West, LA-UR-93-115 (1994).
- [49] M. Iodice *et al.* The CO₂ gas Cherenkov Detectors for Hall-A Spectrometers. NIM A 11841.
- [50] G.J. Lolos *et al.* NIM A385 (1997) 403
- [51] R. Perrino *et al.*, INFN/TC-98-06. February 1998
- [52] R. Perrino *et al.* In preparation
- [53] B. Wojtsekhowski, personal communication
- [54] H. Yokogawa, M Yokoyama, Journal of Non-Crystalline Solids 186 (1995)23-29
- [55] K.Arisaka NIM A 385 (1997) 74

Appendix: Participants

O.K. Baker	G. Kumbartzki
E. Beise	J.J. Kelly
W. Bertozzi	R. De Leo
E. Brash	J. LeRose
H. Breuer	G.J. Lolos
W. Boeglin	D. Mack
C.C. Chang	R. Lourie
N.S. Chant	K. Maeda
J.P. Chen	P. Markowitz
E. Cisbani	S. Nanda
F. Duncan	Z. Papandrea
J.M. Finn	R. Perrino
S. Frullani	R. Ransome
F. Garibaldi	P.M. Rutt
L. Kramer	B. Raue
A. Gasparian	P.G. Roos
S. Gilad	A. Saha
S. Glamazdin	T. Saito
J. Gomez	A. Sarty
C. Glashausser	R. Gilman
G.M. Huber	G.M. Urciuoli
M. Iodice	H. Voskanian
S. Beedoe	B. Wojosetkhowski